Algebraic decomposition of fat and water in MRI

Mathews Jacob, *Member, IEEE,* and Bradley P. Sutton, *Member, IEEE*

Abstract— **The decomposition of MRI data to generate water and fat images has several applications in medical imaging, including fat suppression and quantification of visceral fat. We introduce a novel algorithm to overcome some of the problems associated with current analytical and iterative decomposition schemes. In contrast to traditional analytical schemes, our approach is general enough to accommodate any uniform echo-shift pattern, any number of metabolites and signal samples. In contrast to region-growing method that use a smooth field-map initialization to resolve the ambiguities with the IDEAL algorithm, we propose to use an explicit smoothness constraint on the final fieldmap estimate. Towards this end, we estimate the number of feasible solutions at all the voxels, prior to the evaluation of the roots. This approach enables the algorithm to evaluate all the feasible roots, thus avoiding the convergence to the wrong solution. The estimation procedure is based on a modification of the harmonic retrieval (HR) framework to account for the chemical shift dependence in the frequencies. In contrast to the standard linear HR framework, we obtain the frequency shift as the common root of a set of quadratic equations. On most of the pixels with multiple feasible solutions, the correct solution can be identified by a simple sorting of the solutions. We use a region-merging algorithm to resolve the remaining ambiguity and phase-wrapping. Experimental results indicate that the proposed algebraic scheme eliminates most of the difficulties with the current schemes, without compromising the noise performance. Moreover, the proposed algorithm is also computationally more efficient.**

Index Terms— **linear prediction, harmonic retrieval, fat water decomposition, Sylvester matrix, MRI**

I. Introduction

In medical imaging applications of magnetic resonance imaging, the acquired image is dependent on various chemical species as well as the magnetic field (B0) inhomogeneity. The decomposition of the images into chemical concentrations and the B0 map is crucial for various applications. The main utility of this scheme is the suppression of unwanted signals from species such as fat, which often obscures the underlying pathology [1]. This approach is also used to accurately estimate the fat volume in obesity-induced illnesses [2], [3]. Since the B0 induced frequency shift causes image distortions in many MRI acquisition schemes, a precise estimate of the field map is crucial in obtaining distortion-free reconstructions [4]–[7].

In recent years, there has been renewed interest in Dixon-like water-fat decomposition schemes due to their robustness to B0 and B1 (radio-frequency field) inhomogeneities [8]–[16]. The standard practice is to acquire two or three source MR

images, each with slightly different echo-times. These methods are classified as two or three-point schemes depending on the number of source images used. We focus on three point acquisition in this paper. The source images are processed using analytical or iterative algorithms to estimate the concentrations and B0 field map. These algorithms assume a parametric two-frequency model, where the difference between the frequencies (chemical shift between water and fat) is a known constant (see Fig. 1 for a graphical illustration). This model-based approach enables the estimation of the parameters from fewer source images, thus providing the estimates in a reasonable scan time. However, this approach suffers from two main sources of ambiguity: (a) when uniform echo-shifts are considered, the estimated solutions may suffer from phase wrapping. The range of field-map frequencies that can be uniquely estimated is $[-\frac{1}{4\pi T}, \frac{1}{4\pi T})$, where T is echo-spacing. The estimates of the field-map frequencies that are outside this range will be wrapped back to this fundamental range. (b) the algorithm leads to two feasible solutions on voxels with only one metabolite. When one of the chemicals is absent, either of the two frequencies in the model may fit the single exponential due to the metabolite that is present. Both of these uncertainties cannot be resolved from the measured data; additional prior information has to be used to resolve these ambiguities. For convenience, we will refer to the unique solution in the fundamental range as simply the unique solution in the rest of the paper.

Analytical schemes offer an elegant means to estimate the parameters as simple non-linear functions of the measured samples [8]–[12]. These methods evaluate two roots at every voxel (irrespective of whether both species are present or not). They then use a mixture of heuristic and prior information to resolve the ambiguities [8]–[12]. Since these algorithms are designed for specific echo-shift patterns [8], [9], their extension to arbitrary patterns is not obvious. The echo-shift patterns for which these reconstruction schemes were designed often provide redundant measurements, thus resulting in ambiguous reconstructions [13]. In addition, the extension of these methods to estimate more than two metabolites is also non-trivial. Moreover, the noise performance of these non-linear schemes might be suboptimal.

The IDEAL algorithm formulates the estimation of the model parameters as an optimization problem, where the maximum likelihood (ML) criterion is minimized [13], [14]. This technique uses an iterative optimization scheme to minimize the non-linear criterion. In contrast to the analytical methods, IDEAL assumes a single solution at every voxel. When there are two feasible solutions, it converges to the one of them, depending on the initialization. Moreover, the non-linear ML criterion has several local minima, depending upon the fat-water concentrations and echo-shift parameters [17].

A heuristic scheme to initialize IDEAL and thus avoid these problems has been proposed in [17]. This approach attempts to resolve the uncertainties is by using the prior knowledge of the field map smoothness [17].This scheme estimates the voxels sequentially along a rectangular spiral trajectory. To derive the initialization of the current pixel on the trajectory, it performs a polynomial fit of the already solved pixels in a square neighborhood. While it solves the convergence issues in many cases, it often leads to propagation of errors along the trajectory as explained in [17]. Moreover, there are often very few reliable pixels (in the square neighborhood) in regions close to the edge of the object and noisy regions; this often leads to ill-posed/poor polynomial fit leading to poor initializations as demonstrated in the paper.

To overcome the problems associated with the analytic and iterative schemes, we propose a novel framework for fat-water decomposition. In contrast to the region growing approach of initializing the iterative algorithm with a smooth function to obtain a smooth solution, we propose to impose an explicit smoothness constraint on the final field-map estimate. Due to the non-linear nature of the estimation process, the initialization with a smooth function may not lead to a smooth field map estimate. Besides, the polynomial fitting procedure to derive the field map estimate [17] may be ill-posed at regions close to the edge of the objects. The resulting errors may be propagated along the rectangular spiral trajectory used by the algorithm as explained in [17]. To enforce the smoothness constraint on the final fieldmap estimate, we estimate all the feasible solutions at each voxel. The number of feasible solutions (model order) at each voxel is estimated from the noisy data, prior the the estimation of the solutions. The correct solutions from these feasible sets are then chosen subject to the smoothness constraint. This method is also much more computationally efficient than both the standard IDEAL and region growing IDEAL algorithms.

The estimation of the feasible solutions is based on the harmonic retrieval (HR) frequency estimation theory. This well-established framework is used for the estimation of unknown frequencies in a time domain signal [18], [19]; in the context of MRI, it has been used to estimate the metabolite peak locations [20]–[22], solvent suppression [20]–[23] in MR spectroscopic imaging, and field inhomogeneity estimation [24]. The main contribution of this paper is the modification of the standard HR setup, where the frequencies are assumed to be independent, to introduce the prior knowledge of difference in frequencies of the chemical species. The introduction of this information makes the approach more robust than the standard HR model. Similar approaches (using chemical shift, amplitude constraints, and frequency range) to constrain harmonic retrieval have been investigated in [22]. This approach was designed in the context of MR spectroscopy applications, where large number of time samples were available. Our main focus is to estimate the unknowns from minimal number of samples, where this scheme is not readily applicable. Moreover, [22] assumes unique solutions, which is not true in our case.

We obtain the feasible solutions as the common roots of a set of quadratic equations. This is in contrast to the standard HR setup, where a set of linear equations are solved. Thanks to the well established algebraic theory of polynomials [25]–[27], the model order evaluation and computation of the feasible solutions are efficiently implemented using simple matrix operations. The ambiguity removal procedure picks the correct root from the feasible sets (at each ambiguous voxel), such that a smoothness criterion is minimized. This criterion is only used in selecting the correct component at the ambiguous voxels and hence does not smooth the measured field map as in regularization based schemes. We use a region merging heuristic to derive a computationally efficient scheme to remove the ambiguity and thus to derive the smooth field map estimate. Thanks to the simple matrix manipulations at each voxel to derive the feasible solutions and the region merging step that consider large regions rather than individual pixels, the proposed algorithm provides significant computational savings over standard schemes.

The proposed scheme is general enough to be used with any uniform echo-shift pattern. We also generalize it to accommodate arbitrary number of metabolites and signal samples, thus enabling its use in other problems such as MR spectroscopy. Since the estimation procedure involves simple matrix operations, the algorithm is computationally efficient. Using Monte-Carlo simulations, we show that the benefits associated with the proposed scheme come only at a marginal decrease in noise performance over iterative schemes.

The rest of the paper is organized as follows. In Section II, we review the Dixon decomposition scheme and the harmonic retrieval framework. In Section III, we introduce the novel algorithm. We address the uniqueness of the estimate in Section IV. In Section V, we consider the extension of the algorithm to multiple chemical species (more than 2) and arbitrary number of samples. We validate the fat-water decomposition algorithm and compare its noise performance with the iterative scheme in Section VI.

II. Preliminaries

We will now review the three point Dixon method and the harmonic retrieval framework on which our method is based. We will also define the notations followed in the paper.

A. Dixon decomposition: mathematical formulation

In the standard setup, the signal at each spatial location $\mathbf{x}$ is modeled as

$$s(\mathbf{x}, t) = c_{\text{water}}(\mathbf{x})e^{i\omega(\mathbf{x})t} + c_{\text{fat}}(\mathbf{x})e^{i(\omega(\mathbf{x})+\Delta)t}, \quad (1)$$

where $c_{\text{water}}(\mathbf{x})$ and $c_{\text{fat}}(\mathbf{x})$ are the concentration values of water and fat respectively. Various system non-idealities such as k-space sampling shifts, subject motion and RF effects can lead to spatially varying water and fat phases [28]. Hence, assuming the concentrations to be real quantities may lead to artifacts. The phases of c_{water} and c_{fat} may be modeled to be the same as in [28]. However, we assume them to be complex quantities for simplicity. $\omega(\mathbf{x})$ denotes the frequency shift due to the magnetic field inhomogeneity. Δ is the chemical shift between water and fat peaks; see Fig. 1 for a graphical illustration. The unknowns in (1) are the concentrations

$c_{\text{water}}(\mathbf{x})$ and $c_{\text{fat}}(\mathbf{x})$ and the field-inhomogeneity induced shift $\omega(\mathbf{x})$. Since the estimation procedure treats each voxel independently, we will omit the dependence on the spatial variable $\mathbf{x}$ for simplicity.
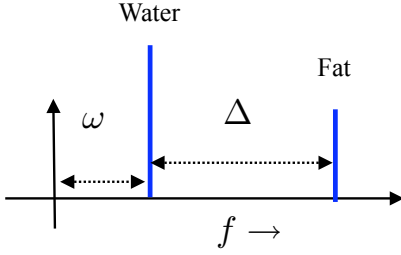
Fig. 1. Water-fat-B0 model. The water and fat peaks are separated by a frequency indicated by Δ corresponding to the chemical shifts between them. Both the peaks are shifted by the field map induced frequency shift ω. The unknowns in the model are the water and fat concentrations (indicated by c_{water} and c_{fat}) and the B0 induced frequency shift (denoted by ω).

The standard practice is to estimate these unknowns from three uniformly spaced samples of the signal, specified by $s(nT + \delta); n = 0, 1, 2$. The sampling step is denoted by T, while δ is a shift parameter to make the echo-shift pattern asymmetric. The Dixon decomposition scheme uses the symmetric echo-shift scheme specified by ($T = \pi/\Delta$, $\delta = -\pi/\Delta$), while the IDEAL scheme assumes an asymmetric pattern ($T = 2\pi/3\Delta$, $\delta = -\pi/6\Delta$). Assuming this pattern, the signal samples are given by

$$s[n] = d_{\text{water}} \left(e^{i\omega T}\right)^n + d_{\text{fat}} \left(e^{i(\omega+\Delta)T}\right)^n, \qquad (2)$$

where $d_{\text{water}} = c_{\text{water}} e^{i\omega\delta}$ and $d_{\text{fat}} = c_{\text{fat}} e^{i(\omega+\Delta)\delta}$. c_{water} and c_{fat} are the concentrations of water and fat respectively. We use the square brackets to distinguish between discrete and continuous domain signals. Note that we model the fat and water signals as undamped exponentials. Since the sampling step T is typically much smaller than the T_2 and T_2^* of the metabolites, this assumption does not affect the estimation.

As discussed before, fitting the two-frequency model, indicated in (1), to a single frequency signal (on voxels with only fat or water present) will result in two feasible solutions. The single exponential may be represented by either of the two frequencies. This is a fundamental ambiguity and can only be resolved by using additional prior information. We will discuss our approach for removing this uncertainty in Section III-D.

B. Frequency estimation using harmonic retrieval

The harmonic retrieval (HR) framework deals with the estimation of unknown frequencies in a signal from its time samples [18]. The framework is rooted on the concept of the annihilating filter. Assume that we have the samples of an exponential given by

$$s[n] = \gamma^n, \qquad (3)$$

where $\gamma = \exp(j\omega); \omega \in \Re$. It is easy to see that the parametric filter (termed as forward annihilating filter)

$$\hat{h}(z) = 1 - \gamma z^{-1} \qquad (4)$$

will annihilate the exponential (3); i.e., $s[n] = \gamma\, s[n-1]$, $\forall n$. Any two consecutive samples of $s[n]$ will provide a linear equation in γ. The unknown parameter γ is estimated from these linear equations. This estimation of the frequency $\omega \in [-\pi, \pi)$ is unique [18] and is also robust [19].

Since $|\gamma| = 1$ (exponential is undamped), the backward filter $1 - \gamma z$ will annihilate the sequence $s^*[n] = \gamma^{-n}$: the conjugate of $s[n]$. This provides an additional set of equations that may be used to improve the robustness of the estimate. We refer the reader to [18] for a more in-depth coverage of the harmonic retrieval framework.

If a two-frequency model is considered, the expression for the signal is given by

$$s_1[n] = c_0 \gamma^n + c_1 \eta^n. \qquad (5)$$

The corresponding parametric filter is given by

$$\hat{h}_1(z) = (1 - \gamma z^{-1})(1 - \eta z^{-1}). \qquad (6)$$

The application of this filter on the time series will provide a set of linear equations in terms of the filter coefficients. In the standard HR framework, the frequencies are obtained as the roots of this polynomial.

III. METHOD

We have seen that the number of feasible solutions is a variable, depending on the number of chemical species present in the voxel. This makes it difficult to implement the estimation procedure as a a one-step algorithm. We propose a sequential approach for the estimation of the field inhomogeneity and the concentration maps. The basic steps involved are:

1) Estimation of the number of feasible solutions (described in Section III-C).
2) Evaluation of the feasible solutions (described in Section III-C).
3) Resolution of the ambiguities (described in Section III-D).
4) Computation of the concentration maps (described in Section III-E).

The resulting algorithm is computationally efficient. Thanks to the algebraic theory of polynomials, the first two steps are performed efficiently using matrix operations. We use a fast, greedy, algorithm to pick the correct root from the feasible solution sets at each ambiguous voxel. Once the field-inhomogeneity is determined unambiguously, the computation of the concentration maps involves the inversion of a system of linear equations.

A. Field map estimation: formulation using HR

Comparing (5) with the fat-water model specified by (1), we find that $\gamma = e^{i\omega T}$ and $\eta = e^{i(\omega+\Delta)T}$. Unlike the standard HR setting, the frequencies in our model (specified by (1)) are related to each other through the relation

$$\eta = \gamma\lambda, \qquad (7)$$

where $\lambda = e^{i\Delta T}$ is a known quantity. This is the central difference between the standard HR framework and the proposed

scheme. We make use of the above relation to derive a filter, parameterized in terms of γ:

$$\begin{aligned} \hat{h}_\gamma(z) &= (1 - \gamma z^{-1})(1 - \gamma \lambda z^{-1}) \\ &= 1 - \gamma(1 + \lambda)z^{-1} + \lambda \gamma^2 z^{-2} \end{aligned} \qquad (8)$$

Since γ and λ are on the unit circle, we can also use the backward relation. The backward filter is given by $h_\gamma\left(z^{-1}\right)$. Applying these filters to the time sequences $s[n]$ and $s^*[n]$, we obtain the following set of quadratic equations in γ:

$$s[n] - (1 + \lambda)s[n-1]\,\gamma + \lambda\,s[n-2]\,\gamma^2 = 0 \qquad (9)$$

$$s[n-2]^* - (1 + \lambda)s[n-1]^*\,\gamma + \lambda\,s[n]^*\,\gamma^2 = 0 \qquad (10)$$

Note that these quadratic equations are valid for any value of n. The actual number of equations at our disposal depends on the number of available signal samples. In three-point Dixon setup, we have three signal samples and hence two quadratic equations. This is the minimum number of samples required to estimate the parameters using this framework. Similarly, we will have four quadratic equations, when four samples are available.

Given the samples $s[n]$, (9) and (10) are the necessary conditions to be satisfied by the solution. We term a solution as feasible, if it satisfies all the equations specified by (9) and (10). Thus, the roots of the greatest common divisor (GCD) of the polynomials will indicate the set of feasible solutions. The number of feasible solutions is obtained as the degree of the GCD polynomial. The GCD thus provides the complete solution to the problem at hand. We will now focus on the evaluation of the GCD.

B. Evaluation of the polynomial GCD

In this section, we restrict ourselves to the three point Dixon scheme for simplicity. We will generalize this scheme to arbitrary number of metabolites and signal samples in Section V. The evaluation of the GCD can be performed in terms of the associated Sylvester matrix [29]. Assume two quadratic polynomials specified by $P(\gamma) = p_0\gamma^2 + p_1\,\gamma + p_2$ and $Q(\gamma) = q_0\gamma^2 + q_1\,\gamma + q_2$. The 4×4 Sylvester matrix associated with these polynomials is given by

$$\mathbf{S}_{P,Q} = \begin{bmatrix} \mathbf{S}_P \\ \mathbf{S}_Q \end{bmatrix}. \qquad (11)$$

The 2×4 submatrix $\mathbf{S}_P$, corresponding to the polynomial $P(\gamma)$, is defined as

$$\mathbf{S}_P = \begin{bmatrix} p_0 & p_1 & p_2 & 0 \\ 0 & p_0 & p_1 & p_2 \end{bmatrix}, \qquad (12)$$

while $\mathbf{S}_Q$ is defined likewise. Post-multiplying the Sylvester matrix by the vector $[\gamma^3, \gamma^2, \gamma, 1]^T$ provides a vector of polynomials. These polynomials serve as a convenient basis for the GCD; pre-multiplication of this vector by $\mathbf{x} = [a_0\ a_1\ b_0\ b_1]^T$ corresponds to evaluating the polynomial $A(\gamma)P(\gamma) + B(\gamma)Q(\gamma)$, where $A(\gamma) = a_0\gamma + a_1$ and $B(\gamma) = b_0\gamma + b_1$. The Sylvester matrix has some nice properties that are very useful for our application:

1) If the GCD of $P(\gamma)$ and $Q(\gamma)$ is a polynomial of degree r, then $\mathbf{S}_{P,Q}$ will be of rank $4 - r$ [30].

2) If $\mathbf{S}_{P,Q}$ is triangulated to row-echelon form using only row operations, then the $(4 - r)^{\text{th}}$ row gives the coefficients of the polynomial GCD [26].

When the signal samples are not corrupted by noise, these properties enable us to estimate (a) the number of feasible solutions and (b) the solutions themselves. We will now focus on the noisy case.

C. GCD estimation when the samples are noisy

When the coefficients of $P(\gamma)$ and $Q(\gamma)$ are corrupted by noise, they may not have any common roots; $\mathbf{S}_{P,Q}$ will be a full rank matrix in this case. Hence, we look for the approximate GCD of the two polynomials [29]. This involves the estimation of the degree of the GCD and the evaluation of the feasible solutions (steps 1 and 2 of our sequential algorithm).

We use the singular value decomposition (SVD) to estimate the rank (and hence the degree of the GCD) of $\mathbf{S}_{P,Q}$ in the presence of noise. Once the rank is estimated, the denoised matrix (denoted by $\mathbf{S}'$) is obtained by truncating the lower singular values. This is a standard procedure in signal processing for rank reduction and matrix denoising[1].

We denote the SVD of the Sylvester matrix as $\mathbf{S}_{P,Q} = \mathbf{U}\boldsymbol{\Sigma}\mathbf{V}^T$. $\boldsymbol{\Sigma}$ is a diagonal matrix, whose singular values are arranged in the descending order; i.e. $(\Sigma_{1,1} \geq \Sigma_{2,2} \geq \Sigma_{3,3} \geq \Sigma_{4,4})$. Similarly, the SVD of the denoised matrix $\mathbf{S}'$ is given by $\mathbf{S}' = \mathbf{U}\boldsymbol{\Sigma}'\mathbf{V}^T$, where $\boldsymbol{\Sigma}'$ is derived from $\boldsymbol{\Sigma}$. We then derive the approximate GCD (whose degree is indicated by r) using the LU factorization of $\mathbf{S}'$ [26]. The GCD estimation procedure involves the following basic steps.

- Perform the singular value decomposition of $\mathbf{S}$: $\mathbf{S} = \mathbf{U}\boldsymbol{\Sigma}\mathbf{V}^T$. Set $\boldsymbol{\Sigma}' = \boldsymbol{\Sigma}$ and $\Sigma'_{4,4} = 0$.
- Threshold the singular value $\Sigma'_{3,3}$ with an appropriate limit parameter. If $\Sigma'_{3,3} = 0$, then $r = 2$. Else $r = 1$.
- Perform LU decomposition of $\mathbf{S}' = \mathbf{U}\boldsymbol{\Sigma}'\mathbf{V}^T$; the $(4 - r)^{\text{th}}$ row provides the approximate GCD of the two polynomials.

We set $\Sigma'_{4,4} = 0$, because we expect at-least one feasible solution to the system of quadratic equations. The threshold for $\Sigma_{3,3}$ is determined experimentally on a large number of acquired MR images (we use a threshold of $0.15 * \Sigma_{1,1}$). The worst-case scenario is when a pixel with a non-unique solution (two zero singular values) is classified as a unique one (single zero singular value). If the single solution in this case is the wrong one, it is not possible to correct it in the subsequent processing steps. In contrast, if a unique pixel is classified as non-unique and one of the solutions is the correct one, the resulting ambiguity can be resolved using the region merging algorithm. Hence, we set the value of the threshold high so as to avoid non-unique regions being labeled as unique. Alternatively, the optimal value of r may be evaluated using the minimum descriptor length criterion [32]. Intuitively, the threshold that is used to determine the number of metabolites

---

[1]This approach does not preserve the Sylvester structure of the matrix. However, it has been shown to be a robust approach and provides reasonably accurate estimates. The quality of the algorithm may be improved by using structure preserving algorithms [31].

in a voxel is a function of the noise variance. Its value is nonlinearly dependent on the minimum concentration of the second metabolite (the one with lower concentration), which is required to provide a unique solution at the specified noise variance.

D. Selecting the solutions from the feasible sets

Performing steps 1 and 2 of the sequential algorithm, described in the previous subsection, provides a feasible solution-set at every pixel. We have seen that there is a fundamental ambiguity when any of the metabolites are absent. For pixels containing only water, the correct solution is the one with the highest field-map value. Similarly, the correct solution is the one with lowest field-map value for pixels containing only fat. In in-vivo applications, it is found that fat often coexists with water. Hence the solution is unique at the fat voxels. In contrast, many pixels will only have water present in it. Thus, the correct solution (on the non-unique pixels) is almost always the one with the highest field-map value. This can be seen from the illustration shown in Fig. 8-a. A major reason for this assumption to be wrong in in-vivo applications is due to phase-wrapping. If the field map is too low at a pixel with only water present, the wrong solution may wrap and thus have a higher field map value. Similarly, if the field-map is too high, the correct solution may wrap and end up being lower in value than the wrong solution.

We use the above assumption (solution with highest field map value is the correct one) to only derive a good initial guess. Starting with this guess, we propose to use the prior knowledge of the smoothness of the field map to resolve both of these uncertainties (non-unique solutions and phase-wrapping). Thus our algorithm is also able to derive the correct solution even if there are pixels with only fat present. We formulate the ambiguity removal problem as the minimization of the global cost function

$$\mathcal{C}(\mathbf{n}, \mathbf{q}) = \sum_{p=0}^{P-1} \left| \nabla \left(\omega_{n(p)} + q(p) \frac{2\pi}{T} \right) \right|^2. \tag{13}$$

Here $\nabla \omega$ indicates the gradient of ω. P is the total number of pixels. $n(p)$ indicates the index of the selected root ($n(p) \in \{0, 1\}$ on ambiguous pixels, while n(p)=0 on the unique pixels). Similarly, the integer $q(p)$ determines the phase offset at the pth pixel. The vectors $\mathbf{n}$ and $\mathbf{q}$ are essentially the unknowns.

The derivation of the optimal $\mathbf{n}$ and $\mathbf{q}$ that minimize (13) is essentially a quadratic integer optimization problem. The evaluation of the exact solution has a prohibitive computational complexity. We have seen that the solution is well-defined in most regions of the image, except for small connected sub-regions where the solutions are swapped or phase wrapped. Hence, we propose to use a region-merging heuristic to derive a computationally tractable algorithm. This greedy technique is a straight-forward extension of the approach pursued in [33] for phase un-wrapping. While more sophisticated optimization schemes such as [34] may provide better results than our approach, we used the greedy strategy due to its ease of implementation. Moreover, this approach worked well in all our experiments.

The criterion (13) depends on the relative indices (difference in indices) between the neighboring pixels. We start by assuming an initial set of regions, where the indices of the roots as well as the phase offsets of all the pixels in the same region are the same. One could start by assuming each voxel as an independent region. However, to reduce the computational complexity, we follow the approach in [33]. We split the image into different connected regions, inside which the phase values remain in a certain interval. This is achieved by partitioning the image into different regions such that the phase values fall in specified ranges (eg. $\ldots, [-2\pi/3, -\pi/3]$, $[-\pi/3, -0], \ldots$). The connected subregions of each of these regions are identified and are assigned a different region number.

With this partitioning and the assumption that the the indices $n(p)$ and the phase offsets $q(p)$ are the same for all pixels in the same region, we rewrite (13) as

$$\mathcal{C}(\mathbf{n}, \mathbf{q}) = \sum_{i=0}^{N-1} \sum_{j=i}^{N-1} \mathcal{C}(i, j) + \mathcal{C}_{\text{res}}, \tag{14}$$

where

$$\mathcal{C}(i, j) = \sum_{m \in R_i; l \in R_j; l \in \mathcal{N}(m)} |\omega_{n(m)} - \omega_{n(l)} + 2\pi(q(i) - q(j))|^2. \tag{15}$$

Here $R_i; i = 0 \ldots N - 1$ denote the different sub-regions and $n(m) \in 0, 1$ indicates the index of the solutions on the mth pixel. $q(m)$ is the integer phase offset of the region R_m. Here $\mathcal{N}(m)$ denotes the set of four neighboring pixels of the pixel m. $\mathcal{C}(i, j)$ is the measure of the discrepancy between the boundary pixels of regions i and j. $\mathcal{C}_{\text{res}}$ is the sum of the discrete differences of the pixels inside the regions. Since $\mathcal{C}_{\text{res}}$ does not play a part in the optimization process, we ignore it in the optimization process. With this criterion, we follow the approach taken in [33]. We sequentially merge pairs of regions, until all the regions are merged. At each step, we compare all the un-merged region pairs and compare the possible relative indices and integer offsets as in [33]. We combine the pair, whose relative indices and offsets if chosen correctly, will provide the maximal decrease in the criterion. This choice ensures the maximal decrease of cost at each region-merging step. The merged region is then considered as a single entity. Since this is a greedy approach, no guarantees regarding the convergence of the criterion to the global minimum can be made. However, this approach works well in all the experiments considered and is computationally efficient. The different steps of the region merging process is illustrated in Fig. 8.

E. Concentration estimation (step 4)

Having derived the field map, the signal samples are linearly related to fat and water concentrations. This is similar to the

procedure followed in [13]. From (2), we have

$$\underbrace{\begin{bmatrix} e^{i\omega\delta} & e^{i(\omega+\Delta)\delta} \\ e^{i\omega(\delta+T)} & e^{i(\omega+\Delta)(\delta+T)} \\ e^{i\omega(\delta+2T)} & e^{i(\omega+\Delta)(\delta+2T)} \end{bmatrix}}_{\mathbf{A}_\omega} \underbrace{\begin{bmatrix} c_{\text{water}} \\ c_{\text{fat}} \end{bmatrix}}_{\mathbf{x}} = \underbrace{\begin{bmatrix} s[0] \\ s[1] \\ s[2] \end{bmatrix}}_{\mathbf{b}}$$

(16)

We estimate the concentrations as

$$\mathbf{x} = \left(\mathbf{A}_\omega^T \mathbf{A}_\omega\right)^{-1} \mathbf{A}_\omega^T \mathbf{b} \tag{17}$$

IV. UNIQUENESS OF THE SOLUTION

In this section, we analyze the uniqueness of the algorithm in the context of three-point fat-water decomposition. Numerical evaluation of the Cramer Rao bounds was used in [14] to derive the optimal shift. In contrast, we use the quadratic relationship (9) to analytically derive the uniqueness condition. We inject the discrete fat-water model, specified by (2), into the forward equation (9) and identify its roots as

$$\hat{\gamma} = \{\gamma, \ \gamma f(q_\rho, \delta, \Delta, T)\}, \tag{18}$$

where $\gamma = e^{i\omega T}$. The first root is the expected solution, while the second one is the expected solution multiplied by a function f that depends on the echo-shift parameters δ and T, the chemical shift Δ, and the fat-water ratio $q_\rho = \rho_{\text{fat}}/\rho_{\text{water}}$. The non-linear function $f(q_\rho, \delta, \Delta, T)$ is given by

$$f(q_\rho, \delta, \Delta, T) = \left(\frac{1 + q_\rho \exp\left(i(\Delta T + \Delta\delta)\right)}{\exp\left(i\Delta T\right) + q_\rho \exp\left(i\Delta\delta\right)}\right). \tag{19}$$

Due to the relation between the coefficients of (9) and (10), the roots of these equations are also related to each other. If y is a root of (9), then $1/y^*$ will be a root of (10). Thus, the first root in (18) is also a root of (10), and hence a feasible solution. The second root will also be a feasible solution if and only if $|f| = 1$. This in turn implies that the feasible solution is unique when $|f| \neq 1$. To study the uniqueness of the solution derived by the proposed approach, we plot the magnitude and phase of f as a function of q_ρ (for different values of δ) in Fig. 2 (a) and Fig. 2 (b) respectively. We assumed that $\Delta T = 2\pi/3$, the optimal value derived in [13].

Note from Fig. 2 that the symmetric case ($\delta = -2\pi/3$) leads to $|f| = 1$, irrespective of the value of q_ρ. This implies that both the roots will be on the unit circle. There will always be two feasible solutions. The second feasible solution will be given by $e^{(\omega_0 T + \angle f)}$, where $\angle f$ is a function of the ratio of fat-water concentrations: q_ρ. Note that this solution will be lagging the actual solution when $\rho_{\text{water}} < \rho_{\text{fat}}$ and will be leading when $\rho_{\text{water}} > \rho_{\text{fat}}$. It is also seen from Fig. 2 that for assymetric echo-shift patterns ($\delta \neq -2\pi/3\Delta$), $|f| = 1$ only when $q_\rho = 0$ or $q_\rho = \pm\infty$. This implies that these patterns lead to unique solutions, unless either fat or water is absent in the voxel ($q_\rho = 0$ or $q_\rho = \pm\infty$). This corresponds to the fundamental ambiguity discussed earlier. Note that in these cases $|f| = 1$. It can also be seen from Fig. 2 (b) that the second solution will lead the original one by $\Delta T = 2\pi/3$, when fat is absent in the voxel (i.e, $q_\rho \to 0$). Similarly, $\angle f$ converges to $-\Delta T$ when water is absent. Thus, if the wrong solution is chosen, the estimates of water and fat will

be swapped. We have thus shown that when both fat and water concentrations are non-zero, all the asymmetric echo-shift schemes provide unique solutions.
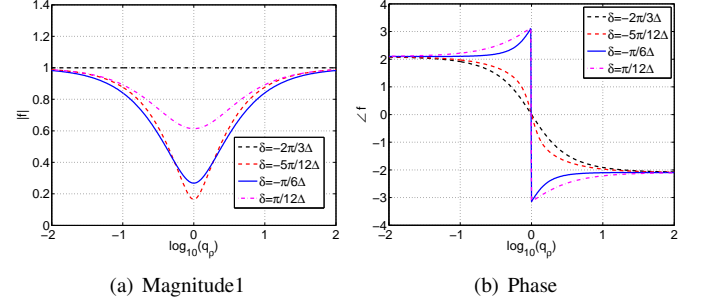
Fig. 2. The magnitude (a) and phase (b) of the non-linear function $f(q_\rho, \delta, \Delta, T)$ as a function of q_ρ. Curves corresponding to four different shift parameters, ranging from $-2\pi/3\Delta$ to $\pi/12\Delta$, at a regular interval of $\pi/4\Delta$ are shown. We assume the optimal sampling step $T = 2\pi/3\Delta$. Note that $|f| = 1$ when $\delta = 0$; the symmetric echo-shift scheme always yields two feasible solutions. The second solution will be lagging or leading the correct root depending on the value of q_ρ. The solution is unique for all the asymmetric patterns, except when $q_\rho \to \pm\infty$. These cases correspond to the voxel containing only water or fat, where the solution is fundamentally ambiguous. When the second solution is close to the unit circle, (when $q_\rho \to \pm\infty$), it may be misclassified to be on the unit circle in the presence of noise. In these worst case scenarios, $|f|$ is farthest from the $|f| = 1$ line, when $\delta = -\pi/6\Delta$.

If $|f|$ is close to unity, the second solution will be close to the unit circle. It may be misclassified as a valid solution in the presence of noise. Thus, the regions close to $q_\rho = \pm\infty$ indicate the worst case scenarios. We see from the plots that $|f|$ is most different from unity when $\delta = -\pi/6\Delta$. It is easy to see that the the optimal shift parameter is invariant to shifts by $2n\pi$. This shift is also the one that provides the most robust solution as shown numerically in [13].

V. GENERALIZATION TO MULTI-METABOLITE AND MULTI-POINT CASES

Our main focus, so far, was on the Dixon-three point decomposition of water and fat. The generalization of the proposed algorithm to arbitrary number of metabolites and number of samples is straight-forward due to the well developed algebraic formalism [25]. These schemes can be used for the MRI exam of the breast with silicone implants as well as MR spectroscopic imaging schemes, where the concentration maps of multiple metabolites have to be derived from the MR data. We will now briefly describe these generalizations.

A. Arbitrary number of metabolites

Assuming the number of metabolite resonances to be M, the discrete model is given by

$$s[n] = \sum_{m=0}^{M-1} d_m \left(\gamma \lambda_m\right)^n, \tag{20}$$

where $\gamma = e^{i\omega T}$, $\lambda_m = e^{i\Delta_m T}$, and Δ_m is the chemical shift of the mth metabolite. $d_m = c_m e^{i(\Delta_m + \omega)\delta}$, where c_m is the concentration of the mth metabolite and $e^{i(\Delta_m + \omega)\delta}$ is a field and chemical-shift induced phase. Note that the observed

(a) Water magnitude   (b) Fat magnitude   (c) Water phase   (d) Fat phase   (e) Field map
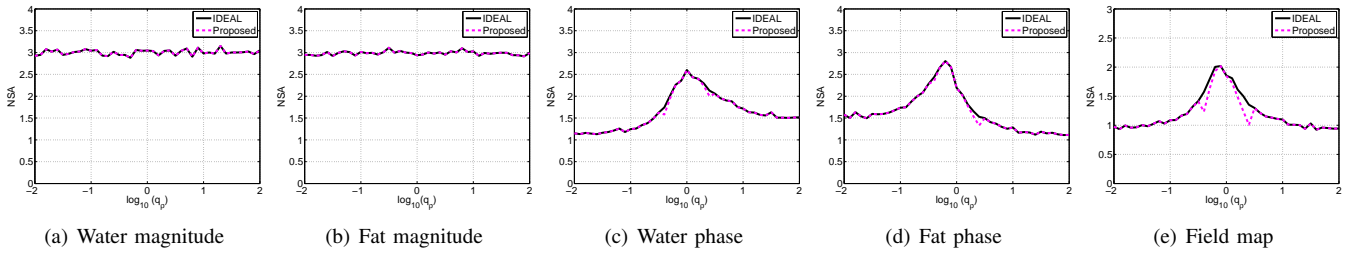
Fig. 3. Noise robustness of the proposed algorithm, in comparison to that of IDEAL. The effective number of signal averages (NSA) vs the fat-water ratio (q_ρ), are plotted. Monte-Carlo simulation with 1000 trials is used to generate the plots. We assumed $\omega\,T = \pi/20$ and the echo-shift pattern specified by $T = 2\pi/3\Delta$, $\delta = -\pi/6\Delta$ to generate the signal samples. Gaussian white noise of a specified variance, such that the SNR=100, was added to the signal samples. Note that the NSA figures of the magnitudes, estimated with the proposed algorithm are exactly the same as IDEAL. The NSA figures corresponding to the phases and the field map is marginally lower than the IDEAL scheme. In short, the results indicates that the noise performance of the algorithm is almost comparable to the IDEAL scheme that is shown to attain the Cramer Rao lower bound.

(a) Used in Fig 5   (b) Used in Fig 6   (c) Used in Fig 7   (d) Used in Fig.8   (e) Used in Fig.9
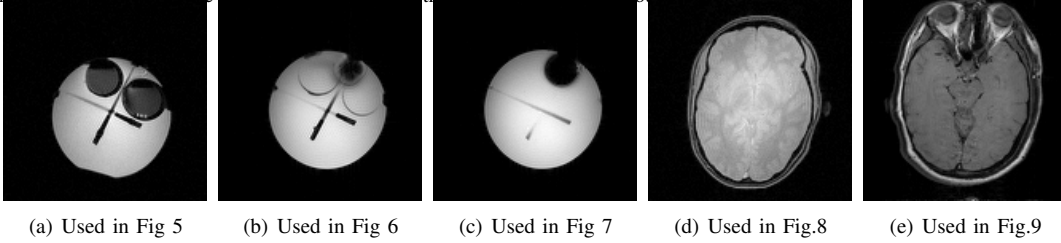
Fig. 4. Source MR images of the slices studied in Figs. 5-9: Three slices of a water-fat-inhomogeneity phantom, acquired using the GRE sequence, are shown in (a)-(c). (a) indicates a slice of the phantom that is the furthest from the air-filled ball and hence has a small field-map dynamic range. It shows the water filled container and the two jars with oil. Fig. (b) and (c) are slices of the same phantom that are closer to the ball. The field-inhomogeneity variations are strong in these slices, especially close to the ball. One of the GRE source images used for the illustration in Fig. 8 is shown in (d). (e) is a source image of the human brain, acquired using a spin echo sequence used to generate the images in Figs. 9.

signal is the sum of M exponentials. The corresponding forward filter is

$$\hat{h}_\gamma(z) = \prod_{m=0}^{M-1} (1 - \gamma\,\lambda_m\,z^{-1}). \tag{21}$$

It is an M-degree polynomial filter, parametrized in terms of the unknown term γ. Applying this filter to the time series $s[n]$, we get the Mth degree polynomial equation:

$$P(\gamma) = \sum_{m=0}^{M} \left(v[m]\,s[n-m] \right)\,\gamma^m = 0, \tag{22}$$

where v_m are the coefficients of the filter $\hat{v}(z) = \prod_{m=0}^{M-1}(1 - \lambda_m z^{-1})$. Similarly, the backward equation provides another M^{th} degree polynomial, denoted by $Q(\gamma)$. Similar to the Dixon three point estimation scheme, the feasible solutions are given by the GCD of these polynomials. The GCD is computed using the $2M \times 2M$ Sylvester matrix, specified by

$$\mathbf{S}_{P,Q} = \begin{bmatrix} \mathbf{S}_P \\ \mathbf{S}_Q \end{bmatrix}. \tag{23}$$

where the $M \times 2M$ submatrix $\mathbf{S}_P$ is given by

$$\mathbf{S}_P = \begin{bmatrix} p_0 & \cdots & p_M & 0 & \cdots & 0 \\ 0 & p_0 & \cdots & p_M & \cdots & 0 \\ \vdots & & \vdots & & \vdots & \\ 0 & 0 & \cdots & p_0 & \cdots & p_M \end{bmatrix}. \tag{24}$$

Similar to the fat-water case considered in Section III, we estimate the degree of the GCD (indicated by r) and the GCD itself from the Sylvester matrix. The degree of the GCD is given by $r = 2M - \text{rank}(\mathbf{S}_{P,Q})$ [25]. The GCD polynomial is obtained by the row echelon decomposition of the matrix,

followed by picking the $(2M - r)^{\text{th}}$ row. Note that the minimum number of signal samples required for the estimation is $M+1$. As in the two metabolite case, the number of feasible solutions is upper bounded by M, depending on the number of metabolites that are present in the voxel. The adaptation of the rank estimation, denoising, and the ambiguity removal algorithm is straightforward and hence will not be discussed. As the number of metabolites increase, the number of feasible solutions may also increase (depending on the location of the metabolite peaks). The extension of the region merging algorithm to this case is straightforward. The computational complexity of the region merging algorithm increases as M^2, where M is the number of metabolites and hence the upper bound on the number of solutions; there are M^2 different possibilities of solution indices between any two non-unique regions.

B. Arbitrary number of samples

We will now generalize the multi-metabolite decomposition algorithm to accommodate more samples. As explained in Section III, the number of available equations also increase with the number of signal samples. This approach can be used to improve the robustness of the estimate. The increased number of samples will also improve the accuracy of the model order estimate. Let us assume that we have L polynomials of degree M indicated by $P_0(\gamma).\ldots,P_{L-1}(\gamma)$. The feasible solutions will satisfy all the polynomial relations $P_l(\gamma) = 0$, $l = 0,\ldots,L-1$. Hence, the solution set is obtained as the roots of the GCD polynomial. The evaluation of the GCD of L polynomials can be performed by using the $LM \times 2M$

generalized Sylvester matrix [25], specified by

$$\mathbf{S}_{(P_0, P_1 \dots P_{L-1})} = \begin{bmatrix} \mathbf{S}_{P_0} \\ \mathbf{S}_{P_1} \\ \vdots \\ \mathbf{S}_{P_{L-1}} \end{bmatrix}, \qquad (25)$$

where each of the submatrices $\mathbf{S}_{P_l}$ are defined as in (24). Thanks to the generalized theory introduced in [25], the GCD and its degree in this case is obtained as in the previous cases. The degree of the GCD (denoted by r) is given by $r = 2M - \text{rank}(\mathbf{S}_{(P_0, P_1 \dots P_{L-1})})$, while the GCD is obtained by reducing $\mathbf{S}_{(P_0, P_1 \dots P_{L-1})}$ to row-echelon form and picking the $(2M-r)^{\text{th}}$ row. Note that the generalized Sylvester matrix is rectangular as opposed to the square matrix in the critically sampled cases considered above. The number of feasible solutions, when the data is non-noisy, is independent on the number of samples. Hence, the computational complexity of the region growing algorithm in this case would be exactly the same as the three point case.

VI. RESULTS

In this section, we validate the fat-water decomposition algorithm using numerical simulations as well as experimental data.

A. Simulation study of noise performance

The IDEAL algorithm minimizes the maximum likelihood criterion and attains the Cramer-Rao lower bounds on the variances of the estimates [14]. In contrast, we resort to a multi-step algorithm to avoid the convergence to wrong solutions and local minima. It may be argued that the proposed scheme may lead to a decrease in noise performance (i.e, increase in variance of the estimates). Hence, in this subsection, we analyze the noise-performance of the algorithm using Monte-Carlo experiments.

For comparisons, we use the effective number of signal averages (NSA) metric, discussed in [9], [14]. This is the traditional measure of noise efficiency in the context of fat-water decomposition [9]; it is defined as

$$\text{NSA}(\hat{\rho}) = \frac{\sigma_s^2}{\sigma_{\hat{\rho}}^2}, \qquad (26)$$

where $\hat{\rho}$ is the magnitude estimate of one of the metabolites, $\sigma_{\hat{\rho}}^2$ its variance, and σ_s^2 the variance of one of Dixon images. The value of the NSA varies from 0 to N, where N is the number of measurements (3 in the three-point Dixon case). The traditional definition is valid only for the magnitude estimates. It has been extended to the other parameters in [14]. For a detailed description, we refer the readers to [14].

We plot the NSA indices for the parameters of interest in Fig. 3. We used 1000 trials to generate the plots. We assumed $\omega T = \pi/20$, $T = 2\pi/3\Delta$, and $\delta = 2n\pi - \pi/6\Delta; n$ integer. The experiments were repeated at different water-fat ratios. Gaussian white noise of a specified variance was added to the samples, such that the SNR of the samples is 100, a reasonable value for SNR of our 3T images. Note that the

NSA indices for the water and fat magnitude for both the algorithms are essentially the same. For the phases as well as the field map, the NSA indices of the proposed scheme is marginally lower than the IDEAL algorithm. Therefore, the benefits of the proposed scheme come only at a negligible loss in robustness.

B. Validation using phantom data

To test the ability of the algorithm to converge to the correct root under controlled conditions, we created a water-fat-inhomogeneity phantom. It consists of an outer container filled with water. Small sealed jars of corn-oil were attached to the interior of the container. We also fixed an air-filled ball to generate a large field map. This phantom was scanned using gradient echo sequence with three different echo times. We used $TR = 500$ms and assumed the optimal echo shift parameters: ($T = 2\pi/3\Delta$ and $\delta = (4\pi - \pi/6)/\Delta$). This translates to TE=3.4 ms, 4.2 ms, and 5 ms respectively. Three slices of the the phantom are shown in Fig. 4.(a)-(c). The slice indicated in Fig. 4.(a) is the furthest from the ball and hence has a small dynamic range for the field map. The slices in Fig. 4.(b)&(c) are close to the ball and hence has a large dynamic range.

The data was processed using the IDEAL algorithm, the region growing IDEAL algorithm and the proposed algorithm. Since the original implementations of IDEAL and region-growing IDEAL were not available, we re-implemented them in MATLAB. For the region growing IDEAL algorithm, we assumed the same parameters[2] (block size of 41×41 and first order polynomial fit) and the same initialization scheme as reported in [17]. The decompositions corresponding to the slices are shown in Fig. 5, Fig. 6 and Fig. 7, respectively. The dynamic range of the field map is small in the Fig. 5 and the iterative algorithm converged to the correct solution. As expected, all the algorithms gave good decompositions of fat and water in this case. In contrast,in Fig. 6, the IDEAL algorithm converged to the wrong solution in regions with large frequency shift, while the algebraic and the region growing methods gave good estimates. In Fig. 7, both the IDEAL and the region growing methods converged to the wrong solution. The proximity of the regions with large field map to the edge of the object led to the region growing algorithm performing poorly. Note that in comparison to the IDEAL, the region growing method propagated the errors to large regions of the image along the rectangular spiral trajectory. The algebraic method worked well in this case as well.

The MATLAB implementation of the algebraic method took around 4 seconds of computation time for a 128x128 image on a 2.33 GHz Intel Core2Duo processor, without any parallel threads. Note that this also included the time taken for the region merging algorithm, which took around 1.8 seconds of the total 4 second computation time. In comparison, the

---

[2]The results of the region growing IDEAL algorithm may be improved with the optimization of the parameters. We varied the block-size without observing much change in the results. However, a rigorous analysis of the performance of this algorithm is beyond the scope of this paper.

standard IDEAL algorithm with 45 iterations on each pixel took around 32 seconds, while our MATLAB implementation of the region growing IDEAL algorithm took 118 seconds. The IDEAL algorithm requires the evaluation and least squares inversion of a 6×4 matrix (with real entries) at every pixel, at each iteration. On the other hand, the algebraic algorithm requires only one evaluation of the SVD of a 4x4 matrix to evaluate the phase value, followed by the least squares inversion of a 3x2 matrix with complex entries. Since our region-merging algorithm starts from a few regions rather than individual pixels, it is very fast.

(a) IDEAL:water   (b) IDEAL:fat   (c) IDEAL:field-map

(d) RG:water   (e) RG:fat   (f) RG:field-map

(g) Algebraic: water   (h) Algebraic: fat   (i) Algebraic: field-map
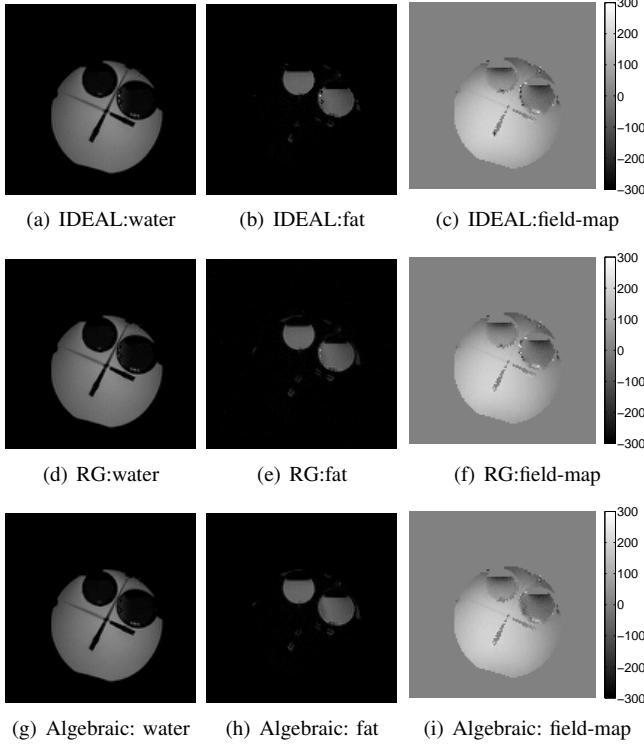
Fig. 5. Fat water decomposition on a water phantom using gradient echo acquisition. One of the source images of this slice is shown in Fig. 4-a. This slice includes the jars containing corn-oil enclosed in the outer container. The cross-section of two plastic combs can also be seen in the image. Since this slice is the farthest from the ball, the magnetic field is relatively homogeneous. In this case, all the algorithms gave good estimates.

(a) IDEAL:Field-map   (b) RG:Field-map   (c) Algebraic:Field-map
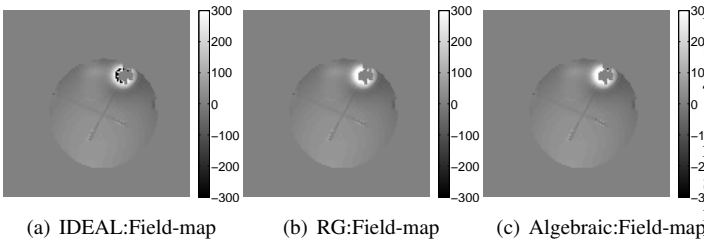
Fig. 6. Fat water decomposition on a water phantom using gradient echo acquisition. One of the source images of this slice is shown in Fig. 4-b. This slice only contains water. Close to the ball, the magnetic field is very in-homogeneous. IDEAL (a) was initialized using zero field map; it converged to the wrong solution. The region growing (b) and the algebraic decomposition algorithms were able to converge to the correct solution. The water and fat images were omitted since no noticeable swapping of intensity is present in any of the images. The value of the signal is pretty small at the voxels where IDEAL converged to the wrong solution.

(a) IDEAL:Water   (b) IDEAL:Fat   (c) IDEAL:Field-map

(d) RG:Water   (e) RG:Fat   (f) RG:Field-map

(g) Algebraic: Water   (h) Algebraic: Fat   (i) Algebraic: Field-map
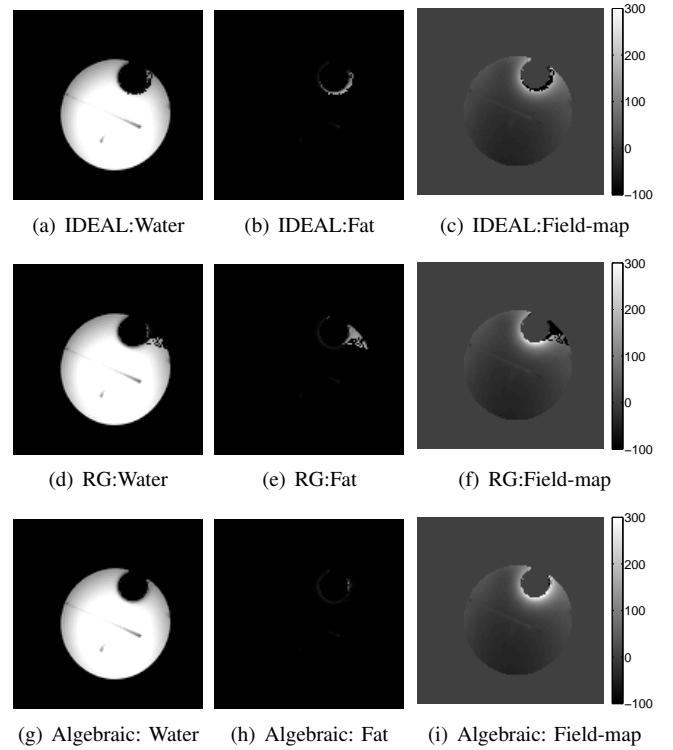
Fig. 7. Fat Water decomposition on a fat-water phantom using gradient echo acquisition. This slice only contains water. One of the source images of this slice is shown in Fig. 4-c. Close to the ball, the magnetic field is very in-homogeneous. The IDEAL algorithm (a-c) was initialized using zero field map; it converged to the wrong solution, resulting in the water and fat signals being swapped in the decomposition. In regions close to the boundary of the object, the region growing algorithm only has information from few reliable pixels to perform polynomial fitting; the initialization is wrong thus leading the convergence of the algorithm to wrong results (d-f). Note the error propagating nature of the region growing algorithm; the wrong estimates are spread to a larger region, along the rectangular spiral trajectory, than the IDEAL algorithm. In contrast to both the standard algorithms, the algebraic algorithm gave pretty good results, correctly identifying the fat and the water signals (g-h). Note that there were a few isolated pixels close to the boundary, where the region merging algorithm failed.

C. Experimental results with brain MR data

We consider two brain data-sets, one acquired using the gradient echo scheme and the other using spin echo method. We used $\delta = -\pi/6\Delta$ for the spin echo and $\delta = 4\pi - \pi/6\Delta$ and gradient echo acquisitions. The repetition times (TR) were chosen as 1200 ms and 500ms respectively. The study was approved by the Institutional Review Board of UIUC and written informed consent was obtained from the volunteers before the study began. The source images are shown in Fig. 4-d&e respectively.

We used the gradient echo acquisition to demonstrate the region merging algorithm in Fig 8. We have adjusted the shim settings to introduce a phase ramp in one direction. This results in the phase map varying from approximately 100 Hz to -400 Hz over the image. The phase map derived by sorting the solutions are shown in Fig. 8-a. Note that this is a good initial guess, with the solutions different from the original values only when there is a phase wrap on the wrong solution. The region merging algorithm divided the image into multiple regions (see Fig. 8-c) and then merged them to obtain Fig.8-d so as to minimize the smoothness criterion. Note that the IDEAL algorithm converged to the wrong solution in regions with

large phase values (Fig.8-e), while the region growing IDEAL was able to avoid this problem (Fig.8-f). In Fig 8.(g)-(h), we compare the solutions derived by IDEAL and the algebraic method at two different voxels. The blue curve indicates the residual error [17]. It is obtained by plotting

$$\mathcal{C}(\omega) = \left| \mathbf{A}_\omega \left(\mathbf{A}_\omega^T \mathbf{A}_\omega \right)^{-1} \mathbf{A}_\omega \mathbf{b} - \mathbf{b} \right|^2 \qquad (27)$$

as a function of the phase value ω. The matrix $\mathbf{A}_\omega$ is the one specified in (16). The IDEAL algorithm converges to the local-minimum of this curve. It is seen that in Fig 8.(h), the algebraic algorithm picked both the feasible solutions. The correct one from this set was selected by the region merging algorithm. In contrast, IDEAL converged to the wrong feasible solution at this pixel.

The spin echo data-set was processed using all the three algorithms (IDEAL, region growing IDEAL, and algebraic) and the results are shown in Fig. 9. Note that both IDEAL and the region growing IDEAL resulted in wrong phase values close to the sinus regions, indicated by the arrows. Also note that the fat and the water regions are swapped. This region corresponds to low signal as well as highly inhomogeneous magnetic field. In contrast, the algebraic algorithm converged to the correct solution, resulting in a smoother field map. The isolated pixels with discontinuous phase map values, derived using the algebraic method, correspond to pixels with low signal. This is confirmed by the fact that water and fat signals are not swapped at these pixels (see g&h).

VII. DISCUSSION

In MR brain imaging, the subcutaneous lipids from the extra-cranial regions generates large signals, which result in many artifacts. It is therefore a common practice to suppress them using preparatory fat-suppression pulses. Unfortunately, this also leads to the suppression of the useful signal, thus affecting the performance of SNR-challenged schemes such as MR spectroscopic imaging. An alternate approach is to constrain the reconstructions using spatial and the field map information, estimated using the Dixon scheme [4]. This is in-fact the application that motivated the development of this approach. However, the main utility of this scheme may be in body imaging, where the field map variations will be considerable [35], [36].

A limitation of the current implementation of the region merging algorithm is its inability to resolve the ambiguity on isolated voxels (separated from the main object). It does not pose a major concern in practical applications since these pixels are usually due to noise (see Fig. 7-i). This limitation is due to the finite difference implementation of the gradient, where only the difference between adjacent pixels is considered. This problem may be minimized by using a criterion that uses smoothed gradients such as $\mathcal{C}(\mathbf{p}, \mathbf{q}) = \sum_p \left| \nabla \left(h \otimes (\omega_{n(p)} + 2\pi q(p)) \right) \right|^2$, where h is a smooth, finitely supported filter (eg. truncated Gaussian). This modification ensures that the evaluation of the smoothed gradient involves more neighboring pixels and hence could propagate the correct solution to isolated voxels.

(a) RG:Water (b) RG:Fat (c) RG:Field map

(d) IDEAL:Water (e) IDEAL:Fat (f) IDEAL:Field map

(g) Algebraic: Water (h) Algebraic: Fat (i) Algebraic: Field map
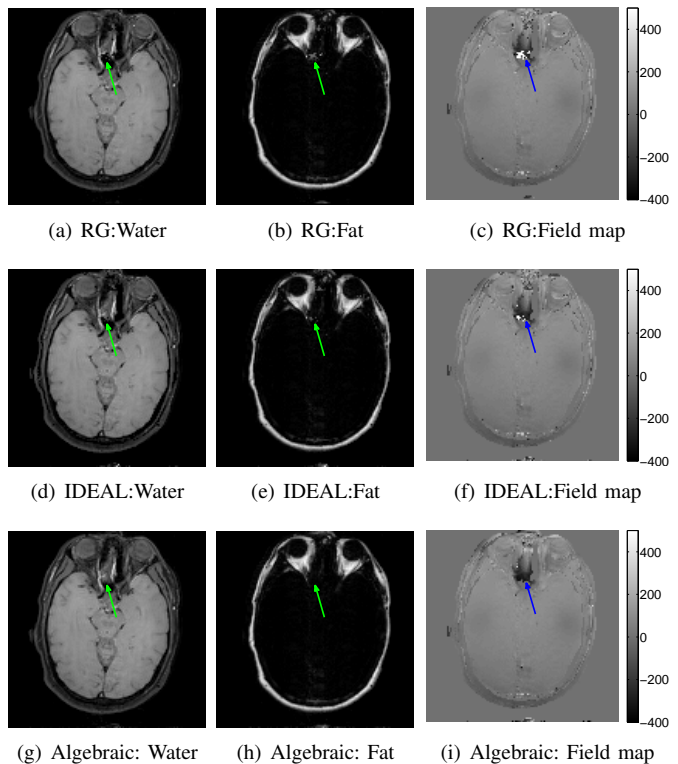
Fig. 9. Fat-water decomposition on SE acquired brain data. One of the source images of this slice is shown in Fig. 4-e. Top row (a-c) indicates the results obtained using the region growing IDEAL algorithm. The second row denotes the decomposition using the IDEAL algorithm. The last row indicates the decomposition using the proposed algebraic method. Note that both the region growing and the IDEAL algorithm converged to the wrong solution close to the sinus regions. This results in fat and water signals being swapped. In contrast, the algebraic method converges to the correct result. We used the optimal shifts derived in [13]; i.e., ($T = 2\pi/3\Delta$ and $\delta = (4\pi - \pi/6)\Delta$) for gradient echo images and $T = 2\pi/3\Delta$ and $\delta = -\pi/6\Delta$ for spin echo images.

Since the algebraic method relies on $\gamma = e^{i\omega T}$ and $\eta = e^{i(\omega+\Delta)T}$ being on the unit circle, it is not possible to extend this algorithm to damped exponentials to account for T_2 or T_2^* effects. However, since the sampling step T that is chosen in practice is often much smaller than T_2 or T_2^*, this is not needed for most applications.

VIII. CONCLUSION

We introduced a general algorithm for the decomposition of water, fat, and field map from Dixon MRI data. The proposed algorithm is based on a modification of the harmonic retrieval framework to accommodate for the frequency shift between the chemical species. We estimated the field inhomogeneity induced frequency shift as the common root of two quadratic polynomials. Using the algebraic framework for the evaluation of the greatest common divisor of polynomials, we developed a computationally efficient algorithm. In contrast to traditional analytical schemes, the algebraic scheme is general enough to accommodate arbitrary equispaced echo-shift patterns, number of metabolites and signal samples. Since the algebraic method estimates all the feasible solutions as opposed to iterative schemes that assume a single solution, it is not affected by the convergence to the wrong solution. Experimental results show that the algebraic scheme eliminated most of the problems

(a) Before region merging   (b) Unique pixels   (c) Regions   (d) After region merging

(e) IDEAL   (f) Region growing IDEAL   (g) Solutions at pixel 1   (h) Solutions at pixel 2
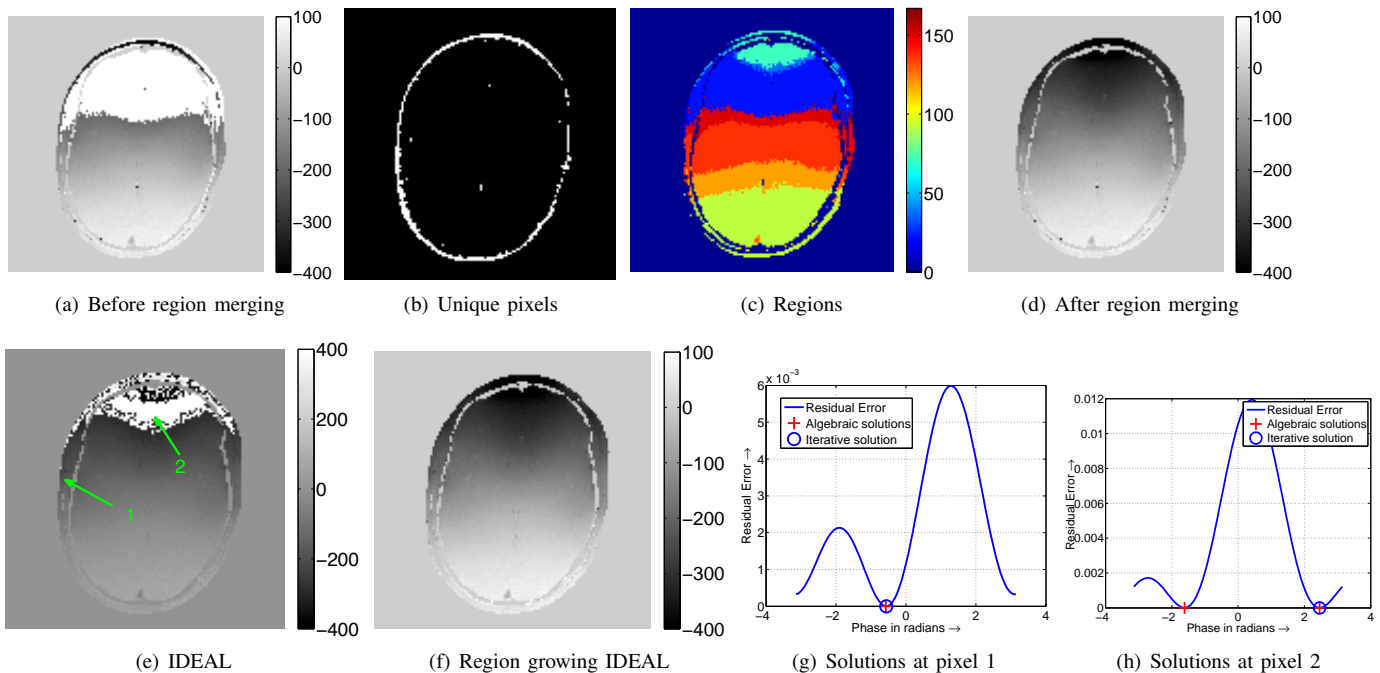
Fig. 8. Illustration of the region merging process. One of the three GRE images of the slice is shown in Fig. 4-d. (a) indicates the phase map before region merging. The pixels on which the solutions are unique are shown in (b). Note that most of the fat pixels are unique. This phase-map image is generated by combining the unique solutions and the solution with a higher field map value (on the non-unique pixels.). Note that this map is close to the final solution (shown in (d)), except for some regions. The region merging algorithm splits the image into simply connected regions with almost the same phase-map value as shown in (c). The different regions are assigned different colors. These regions are merged using the approach discussed above so as to minimize the criterion (13). The solution obtained using the IDEAL algorithm is shown in (e), while the one using region growing IDEAL is shown in (f). Note that the region growing IDEAL gave almost the same result as the algebraic method in this case. The residual error and the solutions obtained using both algorithm at the pixels indicated by the arrows in (e) are shown in (g)-(h). Pixel 1 is identified as a unique pixel by the algebraic method. The corresponding solution is indicated by a red cross in (g). The IDEAL algorithm also converged to the same solution, marked by the black circle. Pixel 2 is identified by the algebraic algorithm as a non-unique pixel. The corresponding solutions are marked by red crosses in (h). Here the low value of the field map led to the wrong solution to wrap and appear as the one with the higher field-map value. However, the region-merging algorithm resolved this problem by picking the one with the lower field-map. In contrast, IDEAL converged to the wrong solution at this pixel, although the correct solution is closer to the initialization. This is because IDEAL is not a gradient based method; the value of ω in IDEAL at each iteration is not updated depending on the gradient of (27). Hence, the gradient of (27) pointing in the correct direction at the initialization is not a sufficient condition for IDEAL to converge to the correct solution. IDEAL converges to the correct solution on this pixel, only if the initialization is below -0.61.

associated with traditional schemes without compromising the noise performance.

REFERENCES

[1] E. de Kerviler, A. Leroy-Willig, O. Clement, and J. Frija, "Fat suppression techniques in MRI: an update." *Biomed Pharmacother*, vol. 52, no. 2, pp. 69–75, 1998.

[2] W. Gong, H. Ren, H. Tong, X. Shen, J. Luo, S. Chen, J. Lai, X. Chen, H. Chen, and W. Yu, "A comparison of ultrasound and magnetic resonance imaging to assess visceral fat in the metabolic syndrome." *Asia Pac J Clin Nutr*, vol. 16 Suppl 1, pp. 339–345, 2007.

[3] D. Armao, J.-P. Guyon, Z. Firat, M. A. Brown, and R. C. Semelka, "Accurate quantification of visceral adipose tissue (vat) using water-saturation MRI and computer segmentation: preliminary results." *J Magn Reson Imaging*, vol. 23, no. 5, pp. 736–741, 2006.

[4] M. Jacob, X. Zhu, A. Ebel, N. Schuff, and Z.-P. Liang, "Improved model-based magnetic resonance spectroscopic imaging," *IEEE Transactions on Medical Imaging*, vol. 26, pp. 1305–1318, 2007.

[5] I. Khalidov, D. Vandeville, M. Jacob, F. Lazeyras, and M.Unser, "BSLIM: Spectral localization by imaging with explicit B0 field inhomogeneity compensation," *IEEE Transactions on Medical Imaging*, vol. 26, pp. 990–1000, 2007.

[6] B. Sutton, D. Noll, and J. Fessler, "Fast, iterative image reconstruction for MRI in the presence of field inhomogeneities," *IEEE Transactions on Medical Imaging*, vol. 22, no. 2, pp. 178 – 188, 2003.

[7] K.S.Nayak and D. Nishimura, "Automatic field map generation and off-resonance correction for projection reconstruction imaging," *Magnetic resonance in medicine*, vol. 43, pp. 151–4, 2000.

[8] W. Dixon, "Simple proton spectroscopic imaging," *Radiology*, vol. 153, pp. 189–194, 1984.

[9] G. Glover and E. Schneider, "Three point Dixon technique for true water/fat decomposition with B0 inhomogeneity correction," *Magnetic resonance in medicine*, vol. 18, pp. 371–383, 1991.

[10] Q. Xiang and L. An, "Water-fat imaging with direct phase encoding," *Journal of Mag Res Imaging*, vol. 7, pp. 1002–1015, 1997.

[11] G. H. Glover, "Multipoint Dixon technique for water and fat proton and susceptibility imaging." *J Magn Reson Imaging*, vol. 1, no. 5, pp. 521–530, 1991.

[12] F. J. Rybicki, R. V. Mulkern, R. L. Robertson, C. D. Robson, T. Chung, and J. Ma, "Fast three-point Dixon MR imaging of the retrobulbar space with low-resolution images for phase correction: comparison with fast spin-echo inversion recovery imaging." *AJNR Am J Neuroradiol*, vol. 22, no. 9, pp. 1798–1802, 2001.

[13] S. B. Reeder, A. R. Pineda, Z. Wen, A. Shimakawa, H. Yu, J. H. Brittain, G. E. Gold, C. H. Beaulieu, and N. J. Pelc, "Iterative decomposition of water and fat with echo asymmetry and least-squares estimation (IDEAL): application with fast spin-echo imaging," *Magnetic resonance in medicine*, vol. 54, no. 3, pp. 636–44, Sep 2005.

[14] A. R. Pineda, S. B. Reeder, Z. Wen, and N. J. Pelc, "Cramér-Rao bounds

for three-point decomposition of water and fat," *Magnetic resonance in medicine*, vol. 54, no. 3, pp. 625–35, Sep 2005.

[15] Q.-S. Xiang, "Two-point water-fat imaging with partially-opposed-phase (POP) acquisition: An asymmetric Dixon method," *Magnetic Resonance in Medicine*, vol. 56, no. 3, pp. 572–84, 2006.

[16] T. E. Skinner and G. H. Glover, "An extended two-point Dixon algorithm for calculating separate water, fat, and B0 images," *Magnetic Resonance in Medicine Magnetic Resonance in Medicine*, vol. 37, no. 4, pp. 628–630, 1997.

[17] H. Yu, S. B. Reeder, A. Shimakawa, J. H. Brittain, and N. J. Pelc, "Field map estimation with a region growing scheme for iterative 3-point water-fat decomposition." *Magnetic resonance in medicine*, vol. 54, no. 4, pp. 1032–1039, 2005.

[18] P. Stoica and R. Moses, *Introduction to Spectral Analysis*. Prentice Hall, 1997.

[19] D. Tufts and R. Kumaresan, "Estimation of frequencies of multiple sinusoids: Making linear prediction perform like maximum likelihood," *Proceedings of the IEEE*, vol. 70, pp. 975– 989, 1982.

[20] H. Barkhuijsen, R. de Beer, and D. van Ormondt, "Improved algorithm for noniterative time-domain model fitting to exponentially damped magnetic resonance signals," *Journal of Magnetic Resonance*, vol. 73, no. 553–557, 1987.

[21] T. Laudadio, Y.Selen, L.Vanhamme, P. Stoica, P. VanHecke, and S. Van-Huffel, "Subspace-based MRS data quantitation of multiplets using prior knowledge," *Journal of Magnetic Resonance*, vol. 168, pp. 53–65, 2004.

[22] P. Stoica, Y. Selén, N. Sandgren, and S. V. Huffel, "Using prior knowledge in svd-based parameter estimation for magnetic resonance spectroscopy–the ATP example." *IEEE Transactions on Biomedical Engineering*, vol. 51, no. 9, pp. 1568–78., 2004.

[23] T. Sundin, L. Vanhamme, P. Van Hecke, I. Dologlou, and S. Van Huffel, "Accurate quantification of H spectra: from finite impulse response filter design for solvent suppression to parameter estimation." J Magn Reson, Aug 1999.

[24] H. M. Nguyen, J. R. L. Morrison, B. P. Sutton, and M. N. Do, "Joint estimation in mri using harmonic retrieval methods," in *Proc. of IEEE International Symposium on Biomedical Imaging*, 2006.

[25] S. Fatouros and N. Karcanias, "Resultant properties of gcd of many polynomials and a factorization representation of gcd," *International Journal of Control,*, vol. 76, pp. 1666–1683, 2003.

[26] K. Geddes, S. Czapor, and G. Labahn, "Another theorem relating Sylvester's matrix and the greatest common divisor," *Mathematics Magazine*, vol. 42, no. 3, pp. 126–128, 1969.

[27] E. Kaltofen and Z. Yang, "Approximate greatest common divisors of several polynomials with linearly constrained coefficients and singular polynomials," in *Proceedings of the 2006 international symposium on Symbolic and algebraic computation*, 2006, pp. 169 – 176.

[28] H. Yu, S. B. Reeder, C. A. Mckenzie, A. C. S. Brau, A. Shimakawa, J. H. Brittain, and N. J. Pelc, "Single acquisition water-fat separation: Feasibility study for dynamic imaging," *Magn. Reson. Med.*, vol. 55, no. 2, pp. 413–422, Feb 2006.

[29] R. Corless, P. Gianni, B. Trager, and S. Watt, "The singular value decomposition for polynomial systems," in *Proceedings of the International Symposium on Symbolic and Algebraic Computation*, 1995, pp. 195–207.

[30] I. Emiris, A. Galligo, and H. Lombardi, "Certified approximate univariate gcds," *J. Pure and Applied Algebra, Special issue of effective methods in algebraic geometry*, vol. 117&118, pp. 229–251, 1997.

[31] E. Kaltofen, Z. Yang, and L. Zhi, "Structured low rank approximation of a sylvester matrix," in *Proceedings of the International Workshop on Symbolic-Numeric Computation SNC 2005*, 2005, pp. 188–201.

[32] J. Rissanen, "Modelling by shortest data description," *Automatica*, vol. 14, pp. 465–471, 1978.

[33] M. Jenkinson, "Fast, automated, N-dimensional phase unwrapping algorithm," *Magnetic resonance in medicine*, vol. 49, pp. 193–197, 2003.

[34] V. Kolmogorov and R. Zabih, "What energy functions can be minimized via graph cuts?" *IEEE Transactions on Pattern Analysis and Machine Intelligence*, vol. 26, no. 2, pp. 147–159, 2004.

[35] A. V. Barger, D. R. DeLone, M. A. Bernstein, and K. M. Welker, "Fat signal suppression in head and neck imaging using fast spin-echo-ideal technique." *AJNR Am J Neuroradiol*, vol. 27, no. 6, pp. 1292–1294, 2006.

[36] S. B. Reeder, M. Markl, H. Yu, J. C. Hellinger, R. J. Herfkens, and N. J. Pelc, "Cardiac cine imaging with ideal water-fat separation and steady-state free precession." *J Magn Reson Imaging*, vol. 22, no. 1, pp. 44–52, 2005.